Journal of Computer Technology and Software

ISSN: 2998-2383

Vol. 4, No. 11, 2025

Machine-Learning-Driven OTA Framework for Spatial Radiation Characterization of RF Circuits

Elena Prokofyeva
University of North Florida, Jacksonville, USA
eprokofyeva87@unf.edu

Abstract: This work addresses the demand for accurate spatial radiation characterization of radio-frequency (RF) circuits and antennas by proposing an OTA (Over-The-Air) test system enhanced with machine learning techniques. The system incorporates a deep learning approach in which a fully connected deep neural network is trained using a limited set of three-dimensional measurement samples. The trained model is then used to estimate the radiation performance of the DUT across all spatial directions.To balance the number of required sampling points and the prediction accuracy of the neural model, a dynamic accuracy-validation strategy is introduced. The system gradually increases the number of training samples until the model reaches the predefined accuracy threshold.Experimental evaluations demonstrate that, compared with conventional OTA measurement systems, the proposed deep-learning-based method can accurately reconstruct the spatial radiation pattern while using only about 60% of the original sampling points. These results confirm the effectiveness, accuracy, and cost-efficiency of the proposed approach, providing a promising solution for low-cost and high-precision spatial radiation testing in RF circuit applications.

Keywords: RF radiation; OTA testing; 3D field reconstruction; neural networks; deep learning

1. Introduction

The spatial radiation characteristics of RF transmitters and receivers serve as critical performance indicators for wireless communication devices, largely determined by the RF front-end circuitry, including antenna subsystems [1-4]. International standardization organizations such as the Telecommunications Industry Association (TIA) and the 3rd Generation Partnership Project (3GPP) stipulate that certified wireless devices must undergo OTA verification within a microwave chamber, where transmission power and reception sensitivity are evaluated across all directions in three-dimensional space [5-6].

Despite its widespread use, existing OTA radiation measurement systems are restricted by chamber size, the number of probes, rotation accuracy, and allowable measurement time, which collectively limit achievable spatial resolution . In many practical scenarios, however, a much finer spatial resolution is required to assess how RF circuits and antenna systems radiate in various directions, particularly for predicting wireless device coverage and reception capabilities in 3D environments.

To enhance resolution, numerous studies have explored larger microwave chambers [7-9] or denser probe arrays [10-11], enabling more spatial sampling and improved reconstruction of radiation patterns. While effective, such approaches demand larger physical spaces, increase system complexity, and significantly raise measurement time and cost.

To alleviate the testing burden, some researchers have proposed using additional probes or extending rotation step lengths, thereby reducing the total number of spatial sampling points and shortening test duration [12-14]. Although suitable for rapid verification tasks, these methods inevitably compromise spatial resolution and measurement accuracy. In parallel, other researchers have investigated near-field compression techniques to infer far-field radiation performance from measurements obtained in compact chambers [15-16]. However, such methods often struggle to accurately approximate the true radiation characteristics at unsampled locations, leading to considerable prediction errors.

To overcome these limitations, this paper proposes a deep-learning-driven OTA radiation measurement framework for RF circuits. The system employs a limited set of 3D measurement samples to train a fully connected deep neural network (FCDNN) that predicts the spatial radiation characteristics of the device under test across the entire three-dimensional domain. Traditional theoretical approximation techniques-such as interpolation and polynomial fitting-often fail to capture the highly nonlinear and complex radiation behavior of RF circuits, as the function space they can represent is fundamentally limited. In contrast, FCDNNs function as universal approximators [17], enabling them to model intricate spatial radiation characteristics with significantly improved accuracy.

Experimental results indicate that the proposed system requires only about 60% of the sampling points used in conventional OTA testing to accurately reconstruct full 3D radiation patterns. This substantially reduces measurement time and cost, providing an efficient and scalable solution for precise radiation characterization in RF applications.

2. Theoretical Analysis

2.1 Radiated Power

The radiated power of an RF circuit system in a microwave chamber represents a key metric for evaluating its uplink transmission performance, as it characterizes how much power is radiated in different directions of the three-dimensional space. The measurement generally includes the effective isotropic radiated power (EIRP) and the total radiated power (TRP). EIRP describes the radiated power level in a specific direction under a given polarization, expressed as the product of the transmitted power and the absolute antenna gain in that direction, and is denoted as $EIRP_p(\theta,\phi)$ in dBm. The subscript $p \in \{\theta,\phi\}$ is used to distinguish between the horizontal polarization θ and the vertical polarization ϕ of the probe antenna during testing.

As illustrated in Figure 1, the coordinates (θ,ϕ) represent a point on the unit sphere in the spherical coordinate system, corresponding to a specific direction in the 3D space. Here, $0 \le \theta \le \pi$ denotes the inclination angle, adjustable by the probe's rotational mechanism, while $0 \le \phi < 2\pi$ denotes the azimuth angle, which is controlled through the rotation table of the OTA measurement system. Since this study focuses on characterizing the spatial radiation distribution, only directional variations in 3D space are considered.

To better illustrate directional variations in three-dimensional space, the coordinate axes x, y, z are also introduced in the diagrams. It is important to note that these axes do not carry dimensional meaning; instead, they serve as references to represent measurement directions in the 3D space. Under a specific test direction, the radiation level measured in the chamber is expressed in dBm.

The fundamental measurement procedure for EIRP can be summarized as follows. Prior to testing, the multi-probe microwave chamber system is calibrated, determining the fixed antenna gain G_s, the feed cable loss L_{RF}, and the free-space path loss L_{PL} inside the chamber. Next, the device under test (DUT) is placed inside the chamber and set to emit at its maximum transmission power. The system then adjusts the rotation mechanism to align the polarization of the probe antenna-either horizontal or vertical-with the selected measurement direction. The EIRP in a given direction is computed as

$$EIRP = P_m + L_{RF} - G_s + L_{PL}$$

where P_m is the average received signal power measured by the probe. Finally, by utilizing multiple spatially distributed probes, the system aggregates directional measurements to obtain the DUT's EIRP over the entire sphere.

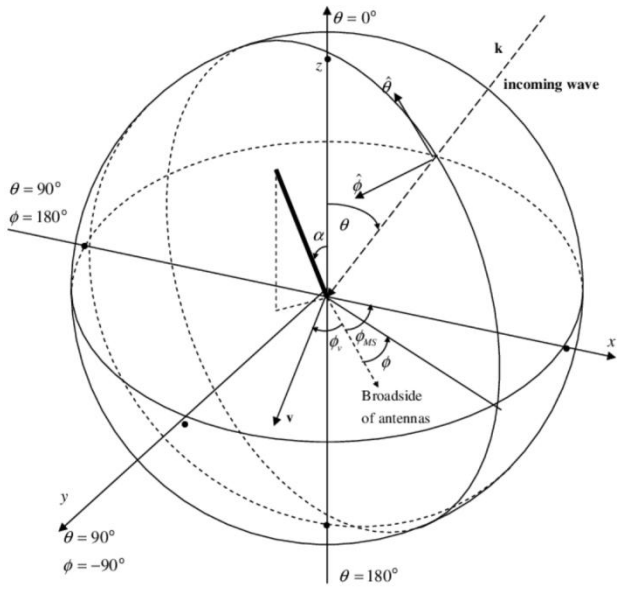

Figure 1. 3D spatial direction and spherical coordinates with unit radius

The effective isotropic radiated power (EIRP) distribution describes how the device under test radiates toward all directions in three-dimensional space, while the total radiated power (TRP) reflects the overall radiation performance integrated over the entire spherical domain. In practice, however, the number of sampling points that an OTA system can measure is typically limited by hardware constraints such as rotation accuracy, mechanical complexity, and the number of available probes. As a result, TRP is usually estimated through numerical integration using a finite set of discrete EIRP measurements rather than through continuous sampling.

When the elevation angle is sampled at N discrete points using N probes, and the azimuth angle is sampled at M rotational positions, the TRP can be approximated by accumulating the EIRP contributions from both horizontal and vertical polarizations at each sampled direction. Under these conditions, the total radiated power measured by the OTA system can be expressed a

$$TRP \approx \frac{\pi}{2NM} \sum_{n=0}^{N-1} \sum_{m=0}^{M-1} \left(EIRP_\theta(\theta_n, \phi_m) + EIRP_\phi(\theta_n, \phi_m) \right) \sin\theta_n$$

where $EIRP_\theta$ and $EIRP_\phi$ denote the horizontally and vertically polarized EIRP values measured at direction (θ_n, ϕ_m). This approximation enables the system to estimate TRP accurately even when the number of sampling points is constrained by chamber hardware limitations.

2.2 Receiving Sensitivity

While the previous subsection focused on radiated power, which primarily reflects the transmission performance of an RF circuit system, the receiver-side performance is equally critical. It is typically characterized by the effective isotropic

sensitivity (EIS) and the total isotropic sensitivity (TIS) of the device . The EIS measurement reflects the minimum detectable signal level at the receiver when the probe antenna transmits toward a specific direction under a given polarization, expressed as $EIS_p(\theta_n, \phi_m)$ in dBm, where $p \in \{\theta, \phi\}$ denotes the horizontal or vertical polarization.

The measurement procedure for EIS generally follows these steps. First, the multi-probe microwave chamber system must be calibrated to determine the fixed antenna gain G_s, the feed cable loss L_{RF}, and the free-space propagation loss L_{PL} inside the chamber. The device under test is then placed on the rotation table, after which the system activates the probe antenna in a particular direction and polarization. The EIS in the direction (θ_n, ϕ_m) is computed as

$$EIS = P_r - L_{RF} + G_s - L_{PL}$$

where P_r is the minimum received power at which the device under test achieves a target bit error rate (BER)-commonly defined as 10%-under the maximum probe transmit power. This minimum transmitted power can be determined by gradually adjusting the probe output level until the BER threshold is met. By combining the probe gain, feed loss, and free-space loss, the receiver sensitivity for the corresponding direction is obtained.

Subsequently, the rotation mechanism is adjusted to activate different probe antennas and polarizations, allowing the system to measure EIS across all spherical directions sampled on the 3D surface. Similar to the relationship between EIRP and TRP, the total isotropic sensitivity (TIS) reflects the overall receiver sensitivity of the device and can be computed by integrating EIS across the entire spherical domain. Its discrete approximation is given by

$$TIS \approx \frac{\pi}{2NM} \sum_{n=0}^{N-1} \sum_{m=0}^{M-1} \left(\frac{1}{EIS_\theta(\theta_n, \phi_m)} + \frac{1}{EIS_\phi(\theta_n, \phi_m)} \right) \sin\theta_n$$

where EIS_θ and EIS_ϕ denote the horizontally and vertically polarized sensitivities at direction (θ_n, ϕ_m).

Unlike (1), equation (2) integrates the reciprocal of EIS. This is because receiver sensitivity varies significantly across directions, and failing to use the reciprocal may cause large sensitivity values to dominate the integral, ultimately producing an overly optimistic estimate of the device's overall receiving performance. The reciprocal-weighted integration ensures a more balanced evaluation of the device's true isotropic sensitivity.

2.3 Proposed Deep Learning-Based Testing Method

To accurately evaluate the EIRP and EIS characteristics of a device under test (DUT) across the entire three-dimensional space-and to subsequently compute its TRP and TIS according to (1) and (2)-existing direct testing approaches typically require selecting a dense set of sampling points on the spherical coordinate grid illustrated in Figure 1. However, in a real microwave chamber, the time required to measure each point is substantial, particularly for EIS measurements, where the probe transmit power must be repeatedly adjusted until the DUT reaches its minimum detectable sensitivity. As a result, it is difficult for current OTA systems to support extremely dense sampling due to high time consumption and measurement cost.

Moreover, direct OTA measurement only provides radiation information at sampled points and lacks an effective modeling method to infer the radiation characteristics at unsampled directions. This often leads to significant estimation errors. Therefore, existing direct methods face substantial limitations: complex testing procedures, high measurement time, and difficulty balancing system cost and accuracy, all of which motivate the development of new testing methodologies.

Based on these challenges, this work focuses on two key questions:

How can we reliably infer the DUT's radiation characteristics at unsampled spatial directions using only the measured samples?

How can we achieve this while significantly reducing the required number of sample points without sacrificing the accuracy of EIRP/EIS prediction?

The proposed deep-learning-based OTA system is designed to address these problems.

Thus, if the designed measurement system can obtain a limited number of spatial samples, and if these data can be used to determine the mapping function $f_E(\cdot)$, the full radiation distribution of the DUT in 3D space can then be reconstructed. However, radiation characteristics of practical RF systems are highly nonlinear, making the mapping difficult to model or approximate using simple analytical expressions.

Fortunately, the success of deep learning-based modeling in related OTA research over recent years [18-19], along with the powerful capability of neural networks to approximate complex nonlinear mappings, provides strong support for the present work. As such, this paper proposes implementing a fully connected deep neural network (FCDNN) to learn the mapping function $f_E(\cdot)$ from limited sample measurements.

The process begins with collecting multiple radiation measurements of the DUT at various locations in the 3D space, obtaining true EIRP/EIS values under real chamber conditions. Next, using the collected dataset, the FCDNN is trained to minimize the mean squared error (MSE) between its predicted outputs and the actual measurement values. The optimization problem is formulated as

$$\min_E \ \mathbb{E}_{\mathbf{x}} \left[\left(\hat{y}_E(\mathbf{x}) - y_E(\mathbf{x}) \right)^2 \right] \approx \frac{1}{|X|} \sum_{\mathbf{x} \in X} \left(\hat{y}_E(\mathbf{x}) - y_E(\mathbf{x}) \right)^2$$

subject to

$$\hat{y}_E(\mathbf{x}) = FCDNN_E(p, \theta_r, \phi_r; \varphi_E)$$

where $\mathbb{E}[\cdot]$ denotes mathematical expectation, X is the set of all measured points, $|X|$ is the total number of samples, $\widehat{y}_E(\mathbf{x})$ is the predicted radiation value, and $FCDNN_E(\cdot; \varphi_E)$ represents the fully connected neural network whose parameters are denoted by φ_E. The subscript E again

distinguishes the EIRP and EIS models. The optimization is solved via stochastic gradient descent (SGD) [20].

Although training with more dense sampling points generally leads to a more accurate model, excessively dense sampling significantly increases OTA measurement time and system cost. Therefore, a balance must be maintained between model accuracy and sampling overhead. Building upon this principle, a dynamic accuracy-validation strategy is introduced to progressively increase the number of training samples until the model meets the target accuracy requirement.

As illustrated in Figure 2, the proposed system first randomly selects N_{test} points in 3D space for measurement. These samples $\{N_{\text{test}}, \mathbf{x}, y_E\}$ are stored in a validation pool for future accuracy evaluation. The system then randomly collects training samples while ensuring that the training set does not overlap with the validation set. If training samples are spatially close to validation samples, the model tends to perform well on the validation set; if training samples are far from the validation samples in 3D space, prediction errors tend to increase. By progressively adding more training samples, the model performance on the validation set can be improved until a certain error margin is met.

The specific training procedure is as follows. First, a small batch of N_{train} measurement samples $\{N_{\text{train}}, \mathbf{x}, y_E\}$ is randomly selected and stored as the initial training set. The system then trains the FCDNN using (5). After training, the model is evaluated on the validation set. Only when the validation MSE falls below the predefined tolerance will the model be accepted; otherwise, an additional batch of N_{train} samples will be collected and added to the training set, after which the model is retrained and revalidated. This procedure repeats until the final model satisfies the accuracy threshold.

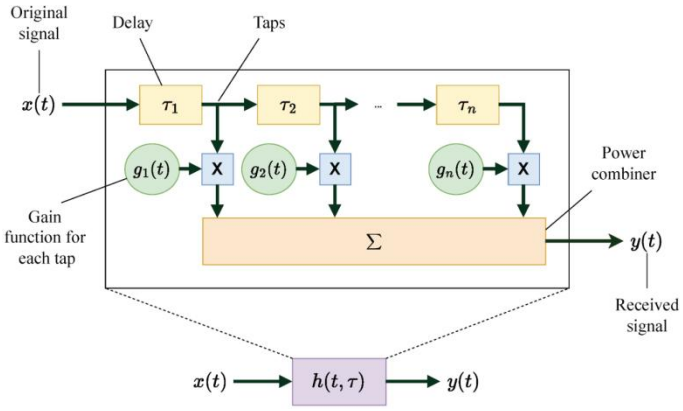

Figure 2. Deep learning-based OTA measurement system for RF circuitries

3. Experiments

3.1 Experimental Environment

In this work, a self-developed multi-probe anechoic chamber (MPAC) system is employed as the experimental test platform. As illustrated in Figure 3, the system primarily consists of a broadband RF communication test instrument, an anechoic chamber, multiple probe antennas, a high-precision turntable and controller, and a computer equipped with an automatic test software suite (ATE). To avoid reflections and multipath interference during spatial radiation measurements, the inner walls of the chamber are lined with absorbing materials, thereby creating an ideal test environment.

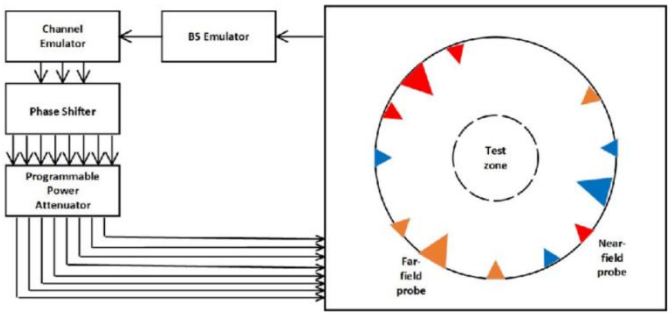

Figure 3. Multi-probe anechoic chamber measurement system

During testing, the device under test (DUT) is placed on the turntable, and the controller rotates the DUT precisely within the horizontal plane to achieve full azimuthal coverage. Perpendicular to this plane, a circular arc frame supports multiple evenly distributed probe antennas, enabling the system to capture the DUT's radiated characteristics across various elevation angles. These probe antennas, together with the rotation and switching mechanisms, interface with the spatial channel emulator and are controlled by the broadband RF communication instrument. This setup enables accurate measurement of the DUT's radiation characteristics in different directions and under various wireless channel conditions.

Finally, communication between the RF instrument and the turntable controller is managed by a personal computer running the custom-developed ATE software. The software provides a unified interface for test configuration, automates data acquisition, and supports real-time visualization and storage of measurement results.

3.2 Experimental Method

To validate the feasibility, efficiency, and accuracy of the proposed deep-learning-based spatial radiation testing framework, an OPPO Reno3 Pro smartphone is selected as the DUT. The experiment focuses on measuring the spatial radiation performance of its 802.11n Wi-Fi transceiver. Specifically, the DUT operates on Channel 1 in the 2.4 GHz band, with a center frequency of 2412 MHz, a system bandwidth of 20 MHz, and a modulation and coding scheme (MCS) of MCS3.

The first step is to use the MPAC system to conduct direct OTA measurements of the DUT's EIRP and EIS values, which serve as the ground truth for evaluating subsequent model performance. Regarding sampling density, two angular resolutions are considered on the spherical grid shown in Figure 1. 30° spacing, and 15° spacing, corresponding to a total

of 120 and 528 measurement points, respectively, when combining both elevation and azimuth directions.

Both horizontal and vertical probe polarizations are included, and the measured EIRP/EIS performance of the DUT is presented in Figure 4. It should be noted that, consistent with Figure 1, the axes in Figure 4 and 5 do not carry physical units. Instead, they represent directional positions in 3D space, and the measured radiation levels in a particular direction are expressed in dBm as depicted by the color scale.

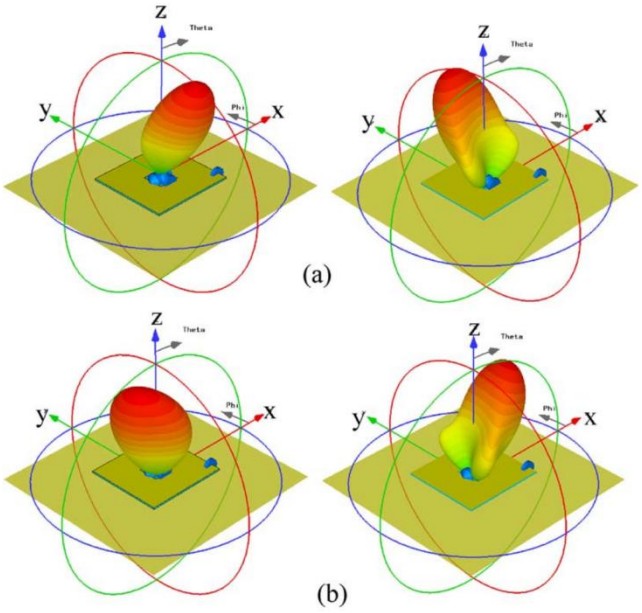

Figure 4. OTA performance of DUT based on the conventional method

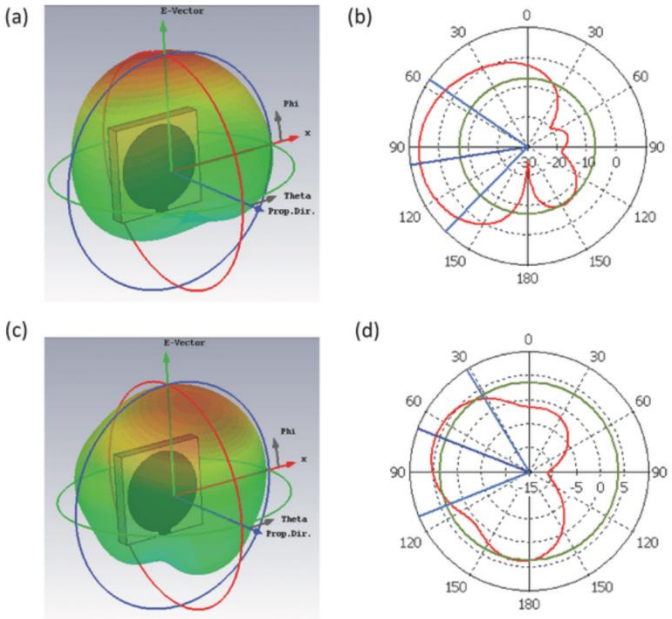

Figure 5. Over-the-air performance of DUT based on the proposed deep learning method

From Figure 4, it can be observed that the DUT exhibits noticeably different radiation strengths across various spatial directions. Moreover, as the sampling density increases, the reconstructed spatial radiation patterns become more refined; however, the large number of sampling points inevitably results in higher measurement time and increased system complexity.

To further evaluate the performance of the proposed deep-learning-based spatial radiation testing method presented in Fig. 2, a series of experiments are conducted. First, 60 randomly selected measurement points ($N_{\text{test}} = 60$) are used to construct the validation set for evaluating model accuracy. For the training set, three different scales of random sampling-140, 280, and 420 points-are considered to form three independent datasets used to examine the model's predictive performance under varying training sample densities.

In the neural network architecture, each neuron employs the rectified linear unit (ReLU) activation function. To obtain a more robust and stable training model, all collected data samples undergo the normalization procedure defined in (6):

$$\hat{a} = \frac{(a - \bar{a})}{\sigma_a}$$

where a represents the original raw measurement value, $\bar{a}$ is the sample mean, and σ_a is the corresponding standard deviation.

The training of each FCDNN model is performed using stochastic gradient descent (SGD) with a learning rate of 0.02, and the number of training epochs is set to 15,000, ensuring that the model fully converges during training.

3.3 Data Analysis

With respect to the neural network architecture, Table 1 summarizes the MSE performance obtained in the validation set for different FCDNN configurations when predicting the EIS metric. Each element in Table 1 corresponds to a specific network configuration in which the number of elements indicates the number of hidden layers, and the value of each element represents the number of neurons in the corresponding layer. Experimental results show that the configuration containing two hidden layers with 64 neurons each yields the best prediction performance among all tested architectures. Therefore, this configuration (64,64) is adopted as the FCDNN architecture for subsequent experiments. When executed on a laptop equipped with an NVIDIA GeForce RTX 3050 Ti, the training of each model takes only a few seconds, indicating that network training does not introduce any computational bottleneck to the overall testing system.

Table 1: Mean squared error (MSE) performance of the trained EIS prediction models under different FCDNN hidden-layer configurations. Each model is trained using 420 samples and evaluated using 60 independent testing samples

FCDNN Hidden-Layer Structure	Testing-Set MSE

{64, 64}	3.8165
{32, 32}	5.8505
{128, 128}	7.8304
{64}	11.7817
{32, 32, 32}	9.0602

Table 2 further compares the MSE performance of FCDNN models trained with different numbers of training samples. As the number of training samples increases, the model becomes more capable of accurately predicting the DUT's spatial radiation characteristics at unmeasured points. Notably, increasing the training samples from 140 to 280 yields a significant improvement in prediction accuracy, whereas the improvement becomes marginal when increasing from 280 to 420 samples. This observation confirms that, to minimize the number of samples required for model training, the proposed dynamic accuracy-validation strategy can effectively determine the appropriate training sample size while maintaining high model accuracy.

Table 2: MSE Performance of Models Trained With Different Numbers of Training Samples (60 Testing Samples)

Number of Training Samples	140	280	420
Testing-Set MSE	8.1035	4.4352	3.7223

Figure 5 illustrates the spatial radiation distributions predicted by the FCDNN models trained with the three different dataset scales. Compared with the densely sampled ground-truth results shown in Figs. 4(b) and 4(d), the predicted radiation patterns closely match the high-resolution direct measurement results, especially as the training sample size increases. When the number of training samples reaches 280, the proposed deep-learning-based method achieves a level of accuracy comparable to that of the direct method using 528 measurement points.

These findings collectively verify the feasibility, efficiency, and accuracy of the proposed deep-learning-based spatial radiation testing framework.

4. Practical Application

In practical application scenarios, Table 3 presents a comparison between the proposed deep-learning-based spatialradiation testing method and the direct measurement method in terms of TRP and TIS values obtained for the DUT. The DUT operates under the following configuration: IEEE 802.11n protocol, Channel 36 in the 5 GHz band, a system bandwidth of 20 MHz, and an MCS index of MCS0. To ensure statistical reliability, each TRP/TIS value reported in the table represents the average of ten independent measurements conducted under the same configuration. The 90% confidence interval is used as the measurement uncertainty range after excluding extreme outliers.

Under the direct measurement approach, two sampling densities are tested:

528 measurement points across the spherical grid

384 measurement points

and the TRP/TIS values are calculated directly from the measured EIRP/EIS distributions.

For the proposed deep-learning-based method, 60 randomly selected points are first used to construct the validation set, while 140 points serve as the initial training set for the system to determine the required number of samples needed for model learning under the MSE threshold. During the test, the system adaptively increases the training set until the validation MSE meets the specified threshold. Based on experimental observations, 280 samples are sufficient to satisfy the required validation accuracy. Considering that some training samples are reused as system verification data rather than pure model-training data, the total sample count required by the proposed method is approximately 340, which is still significantly lower than the number required by direct measurement.

After model training is completed, the predicted EIRP/EIS distributions for the DUT are used to compute the TRP and TIS. The results show that, compared with the direct measurement approach, the proposed deep-learning-based method achieves TRP/TIS accuracy within approximately 60% of the sampling cost used by the direct method. Moreover, under comparable testing conditions, the proposed method yields measurement results close to those obtained by direct measurement, while substantially increasing measurement efficiency and reducing system hardware complexity.

Table 3: Comparison Between Direct and Proposed Methods in Terms of Statistical TRP and TIS Measurements for Different Devices and Number of Measurement Samples

Test Method	Mean / dBm	90% CI / dBm	Mean / dBm	90% CI / dBm	Mean / dBm	90% CI / dBm
	Xiaomi 5		Xiaomi 10s		Huawei Honor 9	
Direct TRP (384 samples)	7.99	[7.75, 8.22]	9.02	[8.81, 9.22]	10.49	[10.34, 10.69]
Direct TRP (528 samples)	8.31	[8.04, 8.50]	9.41	[9.19, 9.60]	10.62	[10.43, 10.74]
Proposed TRP (340 samples)	8.34	[7.94, 8.54]	9.38	[9.10, 9.72]	10.56	[10.22, 10.79]
Direct TIS (384 samples)	−82.06	[−82.17, −81.99]	−85.61	[−86.68, −85.58]	−85.02	[−85.08, −84.90]

Direct TIS (528 samples)	−82.37	[−82.48, −82.30]	−86.09	[−86.08, −85.84]	−85.14	[−85.18, −85.08]
Proposed TIS (340 samples)	−82.40	[−82.65, −82.24]	−86.02	[−86.23, −85.77]	−85.16	[−85.26, −84.94]

5. Conclusion

This paper proposed a deep-learning-based spatial radiation testing system for RF circuits. By leveraging a limited number of measurement samples to train a fully connected deep neural network, the system is able to predict the DUT's radiation characteristics across all directions in the three-dimensional space. Furthermore, to balance the number of required training samples with the prediction accuracy of the model, a dynamic accuracy-validation strategy was introduced to progressively determine the appropriate number of training samples needed for effective model learning.

Experimental results demonstrated that, compared with the conventional OTA testing system requiring 528 measurement points, the proposed method can accurately reconstruct the DUT's spatial radiation characteristics using only about 340 points. In addition, the predicted TRP and TIS results closely match those obtained from the direct measurement method, confirming both the efficiency and accuracy of the proposed approach. In contrast, direct measurement methods suffer from large measurement errors when the sampling density is insufficient.

Overall, the proposed deep-learning-based testing system provides the industry with an efficient, accurate, and low-cost solution for spatial radiation characterization of RF circuits. Finally, future work will focus on exploring more advanced neural network structures and developing higher-order modeling techniques to further enhance system performance.

References

[1] J. Zhang, X. Chen, J. Qi, et al. A survey of OTA testing methods for 5G terminals. IEEE Communications Magazine, 2019, 57(6): 34-41.

[2] S. Zhu, Y. Xie, X. An, et al. Advances in 5G MIMO OTA testing and standardization. IEEE Access, 2021, 9: 115920-115932.

[3] Y. Li, L. Xu, W. Li. Over-the-air test methodologies for 5G base-station antennas. IEEE Antennas and Propagation Magazine, 2018, 60(3): 52-63.

[4] M. Guo, F. Yu, L. Yang, et al. Progress and challenges in 5G MIMO OTA evaluation techniques. Electronics Letters, 2021, 57(12): 489-492.

[5] 3GPP. Verification of radiated multi-antenna performance for user equipment (UE). 3GPP TR 38.827, 2019.

[6] CTIA. Test plan for 2×2 MIMO and transmit diversity OTA performance. CTIA Certification, 2016.

[7] W. Fan, I. Carton, P. Kyösti, et al. OTA evaluation of massive MIMO base stations: challenges and solutions. IEEE Antennas and Propagation Magazine, 2016, 59(1): 38-47.

[8] W. Fan, P. Kyösti, J. Nielsen, et al. Capacity analysis of wideband MIMO channels in multiprobe anechoic chambers. IEEE Transactions on Vehicular Technology, 2015, 65(5): 2861-2871.

[9] P. Kyösti, L. Hentilä, W. Fan, et al. Radiated performance evaluation of massive MIMO devices in multiprobe OTA setups. IEEE Transactions on Antennas and Propagation, 2018, 66(10): 5485-5497.

[10]] A. Khatun, T. Laitinen, V. Kolmonen, et al. Impact of probe count on OTA multiprobe testing accuracy. International Journal of Antennas and Propagation, 2012: 1-10.

[11] A. Khatun, K. Haneda, M. Heino, et al. Feasibility of multi-probe OTA methods above 6 GHz. Loughborough Antennas & Propagation Conference (LAPC), 2015: 1-5.

[12] Y. Qi, P. Jarmuszewski, Q. Zhou, et al. TIS measurement using RSSI-based techniques for wireless terminals. IEEE Transactions on Instrumentation and Measurement, 2010, 59(9): 2414-2419.

[13] P. Shen, Y. Qi, W. Yu, et al. Fast OTA testing for transmit-receive mobile terminals. IEEE Transactions on Electromagnetic Compatibility, 2016, 58(4): 1367-1374.

[14]] I. Llorente, W. Fan, G. Pedersen. MIMO OTA testing in compact multiprobe anechoic chambers. IEEE Antennas and Wireless Propagation Letters, 2015, 15: 1167-1170.

[15] J. Tang, M. Chen, X. Meng, et al. Compact antenna test range using amplitude-phase compensated F/D structures. IEEE Transactions on Instrumentation and Measurement, 2022, 71: 1-14.

[16] Z. Qiao, Y. Xie, Z. Wang, et al. OTA testing for massive MIMO base stations in confined spaces. APCAP 2017: 1-4.

[17] A. Kratsios, B. Ievgen. Universal approximation in non-Euclidean spaces: theory and applications. Advances in Neural Information Processing Systems, 2020, 33: 10635-10646.

[18] L. Song, S. Wang, P. Wang, et al. Intelligent fault diagnosis using deep statistical filtering. Chinese Journal of Scientific Instrument, 2019, 40(7): 39-46.

[19] J. Wen, T. Wang, J. Sun, et al. Pipeline intrusion event detection under complex conditions using deep transfer learning. Chinese Journal of Scientific Instrument, 2019, 40(8): 12-19.

[20] H. Robbins, S. Sutton. A stochastic approximation method. The Annals of Mathematical Statistics, 1951, 22(3): 400-407..